

# TBC: A Target-Background Contrast Metric for Low-Altitude Infrared and Visible Image Fusion

Yufeng Xie, Cong Wang

**Abstract**—Infrared and visible image fusion (IVIF) is a pivotal technology in low-altitude Unmanned Aerial Vehicle (UAV) reconnaissance missions, enabling robust target detection and tracking by integrating thermal saliency with environmental textures. However, traditional no-reference metrics (Statistics-based metrics and Gradient-based metrics) fail in complex low-light environments, termed the “Noise Trap”. This paper mathematically prove that these metrics are positively correlated with high-frequency sensor noise, paradoxically assigning higher scores to degraded images and misguiding algorithm optimization. To address this, we propose the Target-Background Contrast (TBC) metric. Inspired by Weber’s Law, TBC focuses on the relative contrast of salient targets rather than global statistics. Unlike traditional metrics, TBC penalizes background noise and rewards target visibility. Extensive experiments on the DroneVehicle dataset demonstrate the superiority of TBC. Results show that TBC exhibits high “Semantic Discriminability” in distinguishing thermal targets from background clutter. Furthermore, TBC achieves remarkable computational efficiency, making it a reliable and real-time standard for intelligent UAV systems.

**Index Terms**—Image Fusion, Evaluation Metric, Low-Altitude Reconnaissance, Weber’s Law.

## I. INTRODUCTION

**M**ULTI-MODAL perception constitutes the bedrock of situational awareness in modern intelligent surveillance systems. In the specific context of low-altitude Unmanned Aerial Vehicle (UAV) reconnaissance, the visual environment is fraught with challenges, ranging from extreme illumination changes to electronic noise interference. Single-sensor systems often fail to provide comprehensive scene descriptions under such conditions. Infrared (IR) sensors, while robust in capturing the thermal radiation of salient targets (e.g., vehicles, personnel) regardless of lighting [1], suffer from low spatial resolution and a lack of textural definition. Conversely, visible (VI) sensors excel at preserving environmental context and detailed textures [2] but are severely compromised in low-light scenarios. To transcend these physical limitations, infrared and visible image fusion (IVIF) has emerged as a pivotal technology [3], [4]. By synergizing thermal saliency with background texture into a composite representation, IVIF provides high-quality data support that is critical for downstream decision-making tasks, including target detection [5]–[7] and robust tracking [8]–[10].

The evolution of IVIF algorithms over the past decade reflects a paradigm shift from manual signal processing to data-driven representation learning. Early methodologies were dominated by Multi-Scale Transforms (MST) and sparse representation, which decomposed images into base and detail layers for rule-based fusion. With the advent of deep learning, the field has bifurcated into several dominant streams: Auto-Encoder (AE) frameworks that focus on feature extraction and reconstruction [11], Convolutional Neural Networks (CNN) designed for end-to-end mapping [12], [13], and Generative Adversarial Networks (GAN) that model fusion as a distribution alignment problem [14]. More recently, Transformer-based architectures have been introduced to capture long-range dependencies, further pushing the boundaries of visual generation quality [15], [16]. Despite these algorithmic strides, a critical asymmetry persists in the field: *while generation models have become increasingly sophisticated, the evaluation mechanisms used to benchmark them remain archaic*. The community continues to rely heavily on general-purpose No-Reference metrics—such as Entropy (EN) and Average Gradient (AG) [17]–[19]—which were originally designed for undistorted natural images rather than fused imagery in degraded sensing environments.

This study is motivated by a fundamental misalignment between traditional evaluation protocols and the specific requirements of low-altitude reconnaissance. Traditional metrics operate on a statistical hypothesis: “*higher pixel complexity or sharper gradients indicate better image quality*”. While this assumption holds in high-Signal-to-Noise Ratio scenarios, it collapses entirely in low-altitude night environments. In such scenarios, visible images are inevitably plagued by severe high-frequency sensor noise due to high ISO settings [20]. Paradoxically, existing metrics misinterpret this noise as “rich textural information.” We term this phenomenon the “Noise Trap”.

Crucially, our investigation reveals that this failure is not isolated to specific metrics but is a systematic defect across metric families. This paper discusses two metric families. Which one is Gradient-based metrics (e.g., AG, SF), mathematically equating high-frequency noise with texture gradients. And another one is Statistics-based metrics (e.g., EN, SD), mistaking noise-induced histogram spreading for information gain. This evaluation failure misguides the optimization of modern fusion networks. To mitigate this, the research community has witnessed a paradigm shift towards task-driven fusion. Recent prominent works, such as SeAFusion [22], TarDAL [21] and SuerFusion [23] integrate high-level semantic constraints into the fusion framework. Consequently, the performance

Manuscript received x, 2026. (Corresponding author: Cong Wang.)

Y. Xie is with the School of Mathematics and Statistics, Northwestern Polytechnical University, Xi’an, China.

C. Wang is with the School of Mathematics and Statistics, Northwestern Polytechnical University, Xi’an, China (e-mail: congwang0705@nwpu.edu.cn).

of downstream object detection, quantified by mAP, has become a standard for assessing fused images. However, relying solely on mAP for evaluation presents significant dilemmas. It is computationally prohibitive, requires large-scale annotated datasets, and involves heavy inference models. This makes mAP impractical for real-time, unsupervised quality assessment on resource-constrained edge devices.

To resolve this dilemma, this paper aims to establish a lightweight, unsupervised evaluation standard that aligns with machine perception while remaining immune to noise interference. Our technical approach departs from pure statistical measurement, turning instead to psychophysical principles. We propose the **Target-Background Contrast (TBC)** metric, which embeds the “thermal saliency” into the evaluation loop. Specifically, small target detection requires local saliency rather than just global contrast [24]. Therefore, instead of measuring global pixel distributions, TBC focuses on the local semantic contrast of salient targets. By leveraging morphological operations to model the immediate neighborhood of thermal targets, we calculate the relative brightness of the target against its background. This design ensures that the metric selectively rewards the visibility of small targets while imposing a heavy penalty on background noise. Furthermore, thanks to its linear computational complexity, TBC supports real-time evaluation.

The originality of this work lies in the systematic adaptation of Weber’s Law to the domain of low-altitude image fusion evaluation. While Weber’s Law is a foundational principle in psychophysics describing human contrast sensitivity, its application in benchmarking IVIF algorithms has remained unexplored. We bridge this gap by mathematically formulating this physical law into a fusion metric. We demonstrate that the “relative contrast” defined by Weber’s Law is a far more reliable indicator of fusion quality than the “absolute intensity” measured by traditional metrics, particularly in scenarios where the background is dominated by noise. This represents a shift from “signal-level statistics” to “semantic-level perception.”

The main contributions of this paper are summarized as follows:

- It provides a systematic analysis of the failure mechanisms of Gradient-based (AG, SF) and Statistics-based (EN, SD) metrics. It demonstrates, through mathematical derivation (e.g., Rayleigh distribution of noise gradients), that these metrics exhibit a positive correlation with noise intensity, leading to the “Noise Trap”.
- It proposes the Target-Background Contrast (TBC) metric grounded in Weber’s Law. By decoupling target saliency from global background statistics, TBC provides a physically interpretable standard. Large statistical analysis reveals that TBC possesses high “Semantic Discriminability”, whereas traditional metrics exhibit “Semantic Numbness”.
- It designs a comprehensive validation framework based on synthetic degradation and real-world testing. Extensive experiments on the DroneVehicle [25] dataset confirm that TBC achieves superior robustness compared to traditional metrics. Furthermore, TBC demonstrates

remarkable efficiency, making it ideal for real-time UAV applications.

The remainder of this paper is organized as follows. Section II reviews related work on fusion algorithms and evaluation methodologies. Section III details the mathematical formulation of the TBC metric and its theoretical basis. Section IV presents the experimental validation, including synthetic stress tests, real-world statistical analysis, and computational complexity benchmarking. Finally, Section V concludes the paper and discusses future directions.

## II. RELATED WORK

This section reviews the development of infrared and visible image fusion algorithms and the evolution of objective evaluation metrics. Specifically, it analyzes the limitations of existing metrics in low-altitude reconnaissance scenarios and highlight the motivation behind the proposed TBC metric.

### A. Infrared and Visible Image Fusion Algorithms

Over the past decades, image fusion methodologies have witnessed a paradigm shift from traditional signal processing to data-driven deep learning. Early approaches primarily relied on Multi-Scale Transforms (MST), such as Wavelet Transform [26] and Laplacian Pyramid [27], to decompose images and fuse features using manually designed rules. While effective computationally, these methods often struggle with feature representation in complex scenarios.

The advent of deep learning revolutionized this field. Auto-Encoder (AE) based methods, exemplified by DenseFuse [28], introduced learnable feature extraction and reconstruction, significantly improving texture preservation. Subsequently, Generative Adversarial Networks (GAN), such as FusionGAN [14], modeled fusion as an adversarial game to maintain the thermal intensity of infrared targets. More recently, the focus has shifted towards handling long-range dependencies using Transformer-based architectures like SwinFusion [16] and Mamba-based models [29]. Despite these algorithmic advancements pushing visual quality to new heights, the quantitative metrics used to benchmark them have remained largely stagnant, creating a misalignment between generation quality and evaluation standards.

### B. Objective Evaluation Metrics

Since image fusion is typically an unsupervised task lacking Ground Truth, objective evaluation relies heavily on No-Reference metrics. Existing metrics can be broadly categorized into five types [30]. In this paper, we focus on three types of metrics.

1) *Information Theory-based Metrics*: Metrics such as Entropy (EN) [31] and Mutual Information (MI) [32] measure the amount of information contained in the fused image based on statistical distributions. While effective for global assessment, they operate on the assumption that “more complexity equals more information.” In low-altitude night scenarios, high-frequency noise significantly increases the randomness of the pixel distribution. Consequently, EN tends to interpret noise as valid information, assigning high scores to low-quality, noisy images.

2) *Image Feature-based Metrics*: Spatial Frequency (SF) [33] and Average Gradient (AG) [34] quantify texture richness and image clarity by calculating gradient magnitudes. However, as mathematically demonstrated in our experiments, these metrics are highly sensitive to high-frequency components. In low-light environments with low Signal-to-Noise Ratio (SNR), background noise often manifests as strong gradients. Therefore, AG and SF often fall into the “Noise Trap”, failing to distinguish between valid edge details and random sensor noise.

3) *Perception-based Metrics*: Metric like Visual Information Fidelity (VIF) [35] attempts to model the human visual system to assess image naturalness and distortion. Although more robust than statistical metrics, they typically treat all pixels with equal importance or focus on global structural consistency. They fail to account for the specific semantic requirement of reconnaissance tasks — the “relative saliency” of small thermal targets against a cluttered background.

### C. Task-Driven Evaluation

Recognizing the limitations of general-purpose metrics, recent research has shifted towards task-driven evaluation. State-of-the-art methods like SeAFusion [22] and TarDAL [21] incorporate high-level vision tasks (e.g., object detection) into the fusion framework. With the rise of these task-oriented methods, detection accuracy (mAP) has emerged as a de facto standard for evaluating practical utility. However, while mAP accurately reflects machine perception, it presents significant practical challenges. It is computationally prohibitive, requires large-scale annotated datasets, and involves heavy inference models, making it unsuitable for unsupervised, real-time quality assessment.

The proposed **Target-Background Contrast (TBC)** metric bridges this gap. Unlike traditional metrics that are blind to semantics, TBC incorporates the “thermal saliency” inspired by task-driven methods. Simultaneously, unlike mAP, TBC remains unsupervised and computationally efficient (as discussed in Section IV). TBC offers a mathematically sound and physically interpretable standard specifically for low-altitude small target detection.

## III. METHODOLOGY

This section details the theoretical framework of the proposed evaluation metric. First, this paper provides a mathematical derivation explaining the failure mechanism of traditional metrics in noisy environments, categorizing them into statistics-based and gradient-based families. Subsequently, this paper introduces the Target-Background Contrast (TBC) metric, elaborating on its psychophysical foundation, algorithmic formulation, and theoretical properties.

### A. Theoretical Analysis of the “Noise Trap”

Existing no-reference evaluation metrics typically rely on information theory. They assume that high-frequency changes represent valid information. However, this assumption is flawed in low-altitude night scenarios.

To rigorously explain the failure of this metric, we analyze the statistical behavior of traditional metrics under Gaussian noise. It needs to make some necessary assumptions.

This paper assumes that each pixel is independently and identically distributed. Then, the observed visible image  $\mathbf{V}$  is modeled as a superposition of the ideal scene signal  $\mathbf{I}$  and additive sensor noise  $\mathbf{N}$ :

$$\mathbf{V}(x, y) = \mathbf{I}(x, y) + \mathbf{N}(x, y) \quad (1)$$

where  $\mathbf{N}$  typically follows a Normal distribution  $\mathcal{N}(0, \sigma^2)$  caused by ISO sensitivity.

1) *The Statistics-based Family (EN and SD)*: This category of metrics measures the global dispersion or uncertainty of pixel intensities.

a) *Standard Deviation (SD)*: Standard Deviation reflects the dispersion of pixel values relative to the mean intensity. It is mathematically defined as:

$$SD = \sqrt{\frac{1}{MN} \sum_{x=1}^M \sum_{y=1}^N (\mathbf{F}(x, y) - \mu)^2} \quad (2)$$

where  $\mu$  is the mean value of the image. Under this additive model (Eq. (1)), the variance of the observed image follows the additivity property:

$$Var(\mathbf{V}) = Var(\mathbf{I}) + Var(\mathbf{N}) = Var(\mathbf{I}) + \sigma^2 \quad (3)$$

Consequently, the SD score scales with the noise level:

$$SD(\mathbf{V}) = \sqrt{Var(\mathbf{I}) + \sigma^2} \quad (4)$$

As the noise  $\sigma$  increases, SD monotonically rises.

b) *Entropy (EN)*: Entropy quantifies the average information content. For an image  $\mathbf{F}$ , it is defined as:

$$EN = - \sum_{l=0}^{L-1} p_l \log_2 p_l \quad (5)$$

where  $L$  is the number of gray levels, and  $p_l$  is the probability of the occurrence of gray level  $l$ .

According to information theory, a completely random noise signal possesses maximum entropy. In night images, ISO noise flattens the histogram distribution. This artificially inflates the EN score.

When subjected to additive Gaussian noise  $\mathbf{N} \sim \mathcal{N}(0, \sigma^2)$ , the pixel distribution  $P(x)$  spreads out, approximating a Gaussian distribution  $\mathcal{N}(c, \sigma^2)$ . According to information theory, the differential entropy  $H$  of a Gaussian variable is maximized for a given variance and is derived as:

$$EN = H = \frac{1}{2} \log_2(2\pi e \sigma^2) = \log_2(\sigma) + \frac{1}{2} \log_2(2\pi e) \quad (6)$$

Eq. (6) indicates a relationship — the EN score scales with  $\log_2(\sigma)$ . As sensor noise ( $\sigma$ ) increases, the pixel histogram flattens, representing higher statistical “uncertainty.” Traditional metrics misinterpret this noise-induced uncertainty as “information richness,” causing EN scores to rise initially.

2) *The Gradient-based Family (AG and SF)*: This category quantifies texture clarity by calculating gradient magnitudes or frequency responses.

a) *Average Gradient (AG)*: Average Gradient is used to quantify the minute details and texture clarity of an image:

$$AG = \frac{1}{MN} \sum_{x=1}^M \sum_{y=1}^N \sqrt{\frac{\nabla_x \mathbf{F}(x, y)^2 + \nabla_y \mathbf{F}(x, y)^2}{2}} \quad (7)$$

where  $\nabla_x$  and  $\nabla_y$  represent the differences in the horizontal and vertical directions, respectively.

Let  $\nabla$  denote the gradient operator. The gradient of the observed image is:

$$\nabla \mathbf{V} = \nabla \mathbf{I} + \nabla \mathbf{N} \quad (8)$$

Since this paper is mainly investigating the relationship between *AG* and noise,  $\nabla \mathbf{I}$  can be considered a constant. The observed gradient is thus dominated by the noise gradients. By Eq.7, specifically,  $\nabla_x \mathbf{N}(x, y), \nabla_y \mathbf{N}(x, y) \sim \mathcal{N}(0, \sigma^2)$ .

According to probability theory, the magnitude of a vector composed of two zero-mean Gaussian components follows a Rayleigh Distribution.

$$M = \sqrt{\nabla_x \mathbf{N}(x, y)^2 + \nabla_y \mathbf{N}(x, y)^2} \quad (9)$$

By Eq. (7),  $M$  follow a Rayleigh distribution. The scale parameter of this Rayleigh distribution is the standard deviation of the gradients,  $s = \sqrt{2}\sigma$ .

The expected value of the *AG* in noise-dominated regions is therefore derived from the expectation of the Rayleigh distribution:

$$\mathbb{E}[AG] \approx \mathbb{E}[M] = s \sqrt{\frac{\pi}{2}} = (\sqrt{2}\sigma) \cdot \sqrt{\frac{\pi}{2}} = \sqrt{\pi}\sigma \quad (10)$$

Eq. (10) reveals a strict linear relationship — the *AG* score scales proportionally with  $\sqrt{\pi}\sigma$ . So as sensor noise ( $\sigma$ ) increases, *AG* monotonically increases, misleadingly rewarding noisy images with higher quality scores.

b) *Spatial Frequency (SF)*: Spatial Frequency measures the overall activity level of an image based on row frequency (*RF*) and column frequency (*CF*). It is defined as:

$$\begin{aligned} SF &= \sqrt{RF^2 + CF^2} \\ RF &= \sqrt{\frac{1}{MN} \sum (\mathbf{F}(x, y) - \mathbf{F}(x, y - 1))^2} \\ CF &= \sqrt{\frac{1}{MN} \sum (\mathbf{F}(x, y) - \mathbf{F}(x - 1, y))^2} \end{aligned} \quad (11)$$

Mathematically, the terms inside the square are equivalent to *AG*. Therefore, *SF* shares an isomorphic statistical behavior with *AG* under Gaussian noise. As  $\sigma$  increases, the squared differences increase, causing *SF* to scale linearly with the noise level.

In summary, as sensor noise ( $\sigma$ ) increases, both the Statistics-based metrics and the Gradient-based metrics monotonically increase, misleadingly rewarding noisy images with higher quality scores. This phenomenon is termed the “Noise Trap.”

3) *Weber’s Law*: While a whisper is easily audible in a quiet room, a shout might go unheard in a noisy environment. This captures the essence of Weber’s Law, proposed in 1834. It hypothesizes that the ratio of the just-noticeable difference in a stimulus ( $\Delta I$ ) to the background level of the stimulus ( $I$ ) is a constant.

$$k = \frac{\Delta I}{I} \quad (12)$$

Here,  $k$  is known as the Weber fraction, implying that despite variations in  $\Delta I$  and  $I$ , this ratio remains constant.

It suggests that perception depends on relative change, not absolute intensity. Similar concepts are successfully applied in face recognition [36], texture classification [37], illumination compensation [38], [39], and adaptive signal sampling [40].

In the context of low-altitude, the primary task is to detect thermal targets (e.g., vehicles) against a dark, complex background. Therefore, an effective metric should measure the “relative saliency” of the target region with respect to its local neighborhood, rather than the global pixel variance. We formalize this principle into the *TBC* metric.

### B. Formulation of Target-Background Contrast (TBC)

The calculation of *TBC* involves three sequential stages: Salient Target Extraction, Local Background Modeling, and Contrast Computation. Schematic of *TBC* index calculation principle is shown in Fig. 1.

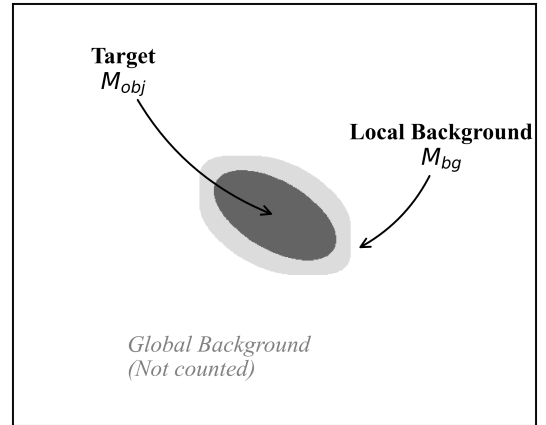


Fig. 1. Schematic diagram of the *TBC* calculation mechanism. The binary mask  $M_{obj}$  (dark gray) denotes the salient target extracted from the infrared prior. The annular region  $M_{bg}$  (light gray), obtained via morphological dilation, represents the local background. *TBC* measures the relative contrast between these two regions, explicitly excluding interference from the distant global background (white area).

#### Step 1: Target Mask Generation

Infrared images ( $I_{ir}$ ) are the most reliable source for locating targets (e.g., vehicles, personnel). Since ground truth annotations are unavailable in unsupervised evaluation, we utilize the infrared image  $I_{ir}$  as a semantic prior. We utilize infrared pixel intensity to generate a binary target mask  $M_{obj}$ :

$$M_{obj}(x, y) = \begin{cases} 1, & \text{if } I_{ir}(x, y) \geq T_{perc} \\ 0, & \text{otherwise} \end{cases} \quad (13)$$

where  $T_{perc}$  is the  $k$ -th percentile of the infrared pixel intensity (set to  $k = 98$  in this work). This ensures only the brightest thermal regions are selected.

### Step 2: Local Background Extraction

We need to define the “immediate background”. Global background includes irrelevant clutter. By applying a morphological dilation operation to the target mask  $M_{obj}$  and subtracting the original target region, we obtain an annular background mask  $M_{bg}$  surrounding the target:

$$M_{bg} = \text{Dilate}(M_{obj}, \mathcal{K}) - M_{obj} \quad (14)$$

where  $\mathcal{K}$  is a  $5 \times 5$  structural element. This definition avoids interference from distant background clutter, ensuring that contrast calculation occurs strictly between the target and its immediate surroundings.

### Step 3: Contrast Calculation

Based on the generated masks, we calculate the average gray values of the fused image  $F$  in the target and background regions, respectively:

$$\mu_{obj} = \frac{\sum F \cdot M_{obj}}{\sum M_{obj}}, \quad \mu_{bg} = \frac{\sum F \cdot M_{bg}}{\sum M_{bg}} \quad (15)$$

Finally, TBC is defined as the relative luminance gain:

$$TBC = \frac{\mu_{obj} - \mu_{bg}}{\mu_{bg} + \epsilon} \quad (16)$$

where  $\epsilon$  is a minimal constant to prevent division by zero.

### C. Theoretical Properties of TBC

Unlike traditional metrics, TBC possesses distinct mathematical properties that ensure its reliability in degraded scenes. The main properties of this paper are summarized as follows:

- Consider a fused image contaminated by zero-mean additive noise in the background region. Since noise typically increases the mean intensity of dark backgrounds (due to non-negative pixel constraints), the denominator in Eq. (16) increases. Consequently,  $TBC$  will decrease. This property mathematically guarantees that TBC penalizes background noise, effectively avoiding the Noise Trap.
- If a fusion algorithm fails to preserve thermal information, the pixel intensity of the target region drops to the level of the visible background, i.e.,  $\mu_{obj} \approx \mu_{bg}$ . In this case,  $TBC \approx 0$ . This property allows TBC to explicitly flag target loss failures, which EN or AG cannot detect.
- By using the ratio of differences, TBC is relatively invariant to global illumination changes, focusing purely on the local contrast structure. This aligns with the requirement of robust reconnaissance under varying lighting conditions.

## IV. METRIC VALIDATION

Validating a metric without Ground Truth is challenging. Direct comparison on real algorithms risks circular reasoning. Therefore, we design a controlled experiment using synthetic degradation. The rationality of this experimental design is primarily reflected in the following two aspects.

For one thing, the output of real fusion models typically mixes various distortions such as contrast loss, edge blurring, and residual noise. For another, by using synthetically generated cases, we can apply the control variable method to independently simulate single variables like “target loss”, “background noise”, and “low contrast”, thereby precisely analyzing the metric’s sensitivity to specific degradation types. By constructing clear “Ideal Fusion” and “Severe Lost” samples, we establish a scientifically benchmark to satisfy the monotonicity assumption. That is, when image quality degrades significantly, the metric value should exhibit monotonic decay.

### A. Experimental Setup

We select typical low-altitude night scenes from the DroneVehicle dataset [25] as a baseline to construct four representative cases: (A) Ideal Fusion, (B) Target Lost, (C) Noisy, and (D) Low Contrast. These four cases are synthetically generated as follows:

- Ideal** This case integrates the raw infrared target directly into a clean, noise-free visible background, representing the theoretical upper bound of fusion quality.
- Loss**: This case retains the visible background but significantly attenuates the infrared target intensity, simulating the failure to preserve thermal saliency.
- Noisy**: Gaussian noise is injected into the Ideal case to simulate high-frequency sensor artifacts common in low-light conditions.
- Low Contrast**: Both the target and background intensities are artificially brightened, reducing the relative saliency and simulating overexposure.

To ensure generalization, this paper conduct tests on all of the DroneVehicle dataset. It chooses only five samples to show its ideas (Fig. 2–6). And this paper use data processing methods such as box plots to present the indicator results. And we verify the formula (Eq. 16) through noise degradation experiments. Furthermore, this paper discusses the selection of parameter values and time complexity.

All experiments are conducted on a standard computing platform equipped with an Intel Core i5-14500 CPU (2.60 GHz), ensuring the reproducibility of the efficiency benchmarks.

### B. Result Analysis

Table I shows the results for Sample 00942 ( $\uparrow$  indicates that higher values represent better quality). Table II shows the results for Sample 03893. (The other three samples are not shown.) Using a single sample cannot adequately demonstrate the validity of the experiment. Therefore, this paper randomly select 300 samples from the total sample to conduct experiments. The experimental data reveal the severe flaws of existing metrics and the superiority of TBC.

This paper first conduct a microscopic analysis on representative samples. Tables I and II present the quantitative results on two distinct scenarios: a typical low-light night scene (Sample 00942) and a complex daytime bridge scene (Sample 03893).

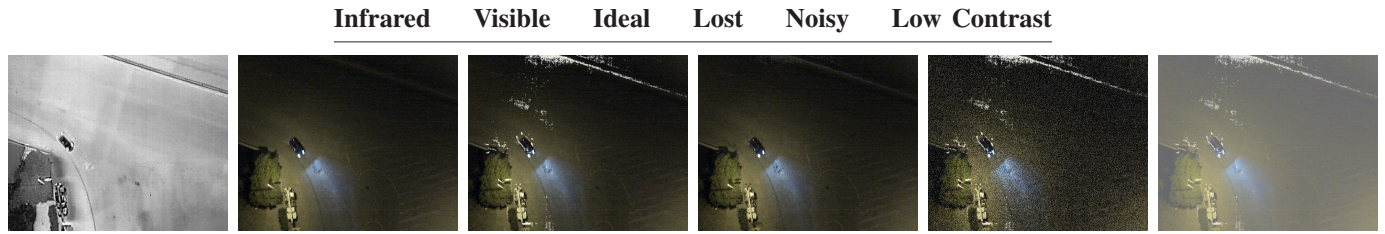


Fig. 2. Visualization of different image types for sample 00942 from the DroneVehicle dataset. Columns represent infrared, visible, ideal, lost, noisy, and low contrast images respectively.

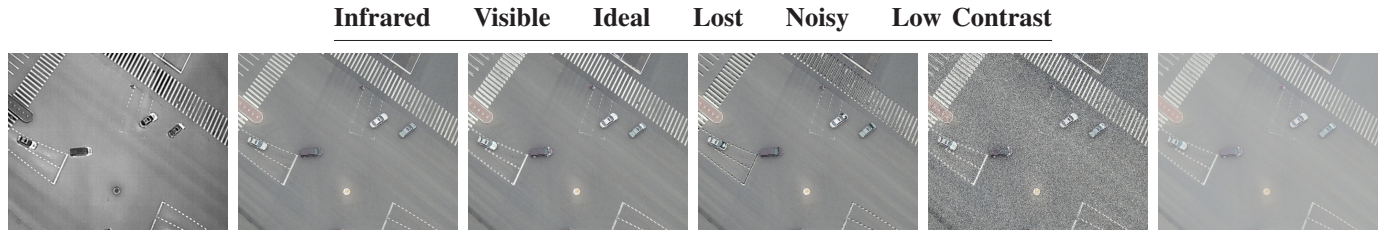


Fig. 3. Visualization of different image types for sample 02994 from the DroneVehicle dataset. Columns represent infrared, visible, ideal, lost, noisy, and low contrast images respectively.

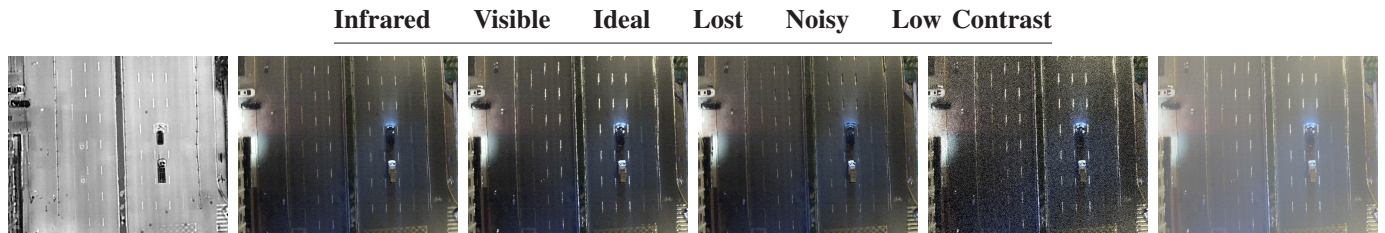


Fig. 4. Visualization of different image types for sample 03813 from the DroneVehicle dataset. Columns represent infrared, visible, ideal, lost, noisy, and low contrast images respectively.



Fig. 5. Visualization of different image types for sample 03893 from the DroneVehicle dataset. Columns represent infrared, visible, ideal, lost, noisy, and low contrast images respectively.

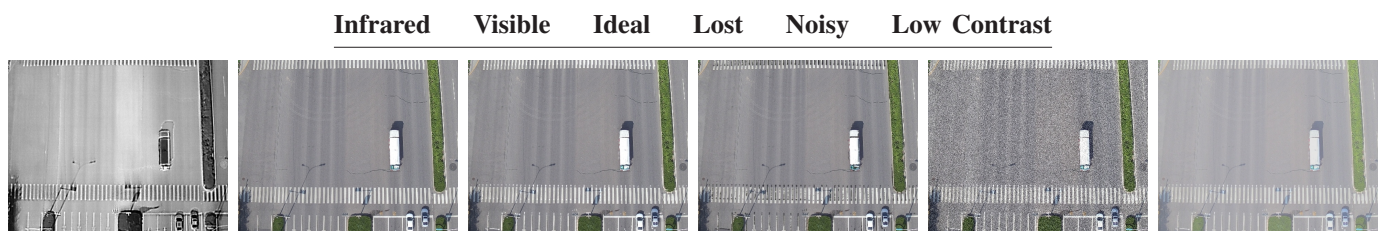


Fig. 6. Visualization of different image types for sample 04834 from the DroneVehicle dataset. Columns represent infrared, visible, ideal, lost, noisy, and low contrast images respectively.

TABLE I  
COMPARISON OF METRIC PERFORMANCE ON SAMPLE 00942

Case	TBC (Ours)	AG	SD	SF	EN
Ideal	2.185	0.122	0.130	0.057	6.619
Lost	-0.081	0.089	0.108	0.037	6.478
Noisy	<b>2.191</b>	<b>0.491</b>	<b>0.198</b>	<b>0.305</b>	<b>6.621</b>
Low Contrast	0.456	0.061	0.065	0.029	5.620

TABLE II  
COMPARISON OF METRIC PERFORMANCE ON SAMPLE 03893

Case	TBC (Ours)	AG	SD	SF	EN
Ideal	0.609	0.200	0.212	0.088	7.241
Lost	-0.345	0.196	0.199	0.088	7.195
Noisy	<b>0.610</b>	<b>0.536</b>	<b>0.260</b>	<b>0.312</b>	<b>7.758</b>
Low Contrast	0.256	0.100	0.106	0.044	6.242

TABLE III  
METRIC PERFORMANCE (MEAN  $\pm$  STD) FOR DIFFERENT CASES

Case	TBC		AG		SF		EN		SD	
	mean	std	mean	std	mean	std	mean	std	mean	std
Ideal	<b>3.042</b>	<b>3.951</b>	0.161	0.062	0.074	0.023	6.436	1.110	0.155	0.044
Lost	0.427	1.699	0.140	0.069	0.061	0.030	6.337	1.138	0.128	0.056
Noisy	2.021	1.870	<b>0.445</b>	<b>0.079</b>	<b>0.268</b>	0.039	<b>6.686</b>	1.075	<b>0.196</b>	0.039
Low Contrast	0.431	0.189	0.080	0.031	0.037	0.012	5.440	1.106	0.078	0.022

A cross-comparison reveals a consistent failure mode in traditional metrics. Specifically, gradient-based metrics (AG, SF) exhibit a pathological sensitivity to noise. For instance, in the ‘Noisy’ case of Sample 00942, the scores of AG and SF surge to 0.491 and 0.305, approximately four to five times higher than their scores in the ‘Ideal’ case. This is experimentally confirmed that gradient operators are mathematically incapable of distinguishing between the structural edges of the scene and the random fluctuations of noise.

Similarly, statistics-based metrics (SD, EN) consistently assign their highest scores to the ‘Noisy’ case. For instance, in the ‘Noisy’ case of both Sample 00942 and Sample 03893, EN and SD both score the highest. These metrics misinterpret noise-induced histogram spreading as valid information gain. So, that’s why ‘Low Contrast’ case has the lowest SD and EN.

In stark contrast, the proposed TBC metric demonstrates remarkable robustness. While random noise fluctuations may cause slight oscillations due to the stochastic brightening of pixels, TBC avoids the “score explosion” observed in AG. More importantly, in the ‘Lost’ case, TBC responds with negative or near-zero values, effectively flagging the semantic loss of targets. This is an excellent capability completely absent in statistics-based metric.

To rule out selection bias, we extended the evaluation to 300 randomly selected samples from the DroneVehicle dataset. The aggregated results, summarized in Table III and visualized in Fig. 7, provide decisive evidence of the metric’s validity. TBC emerges as the sole metric that correctly ranks the ‘Ideal’ case (Mean=3.042) significantly higher than the ‘Noisy’ case (Mean=2.021). Also, in ‘Lost’ case, TBC is very low (Mean=0.427). This clearly reflects the sensitivity of TBC to the target. Similarly, this statistical trend confirms that, at the dataset level, TBC effectively penalizes background noise.

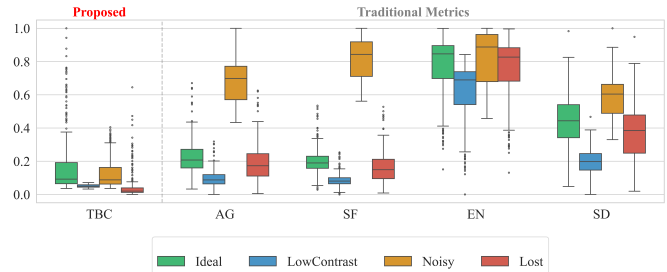


Fig. 7. Systematic comparison of metric responses to synthetic degradation (N=300). The boxplots visualize the statistical distribution of scores for the proposed TBC and four traditional metrics across diverse cases. (Left) TBC correctly assigns significantly higher scores to the ‘Ideal’ case (green) compared to the ‘Noisy’ case (yellow), demonstrating its valid discriminative power. (Right) Traditional metrics (AG, SF, EN, SD) exhibit a systematic failure, consistently rating the ‘Noisy’ case higher than or equal to the ‘Ideal’ case, confirming their susceptibility to the “Noise Trap”.

Conversely, AG, SF, SD, and EN all incorrectly identify the ‘Noisy’ case as the best-performing category (highlighted in red). So, the “Noise Trap” is a systematic defect rather than an isolated anomaly.

Furthermore, the analysis of variance offers profound insights into the physical interpretability of the metrics. A crucial observation from Table III is that TBC exhibits a relatively high variance in the ‘Ideal’ case (std=3.951). From a theoretical perspective, this high variance in TBC should be interpreted as “Semantic Discriminability” rather than instability. The DroneVehicle dataset inherently contains targets with vast differences in thermal intensity, ranging from active engines of truck to cold little vehicles. TBC physically measures this relative contrast, thus faithfully reflecting the real-world diversity of thermal signatures. In contrast, traditional metrics show extremely low variance. The low variance suggests a “Semantic Numbsness”. These metrics treat different semantic targets and random noise indiscriminately as gradients or entropies. This is fatal for low-altitude tasks.

### C. Discussion

This section will supplement the previous experiments with some discussions: Noise degradation, Sensitivity analysis, and Time complexity.

1) *Noise degradation*: As image quality objectively degrades, the metric score should decrease monotonically. To verify this, this paper conduct noise degradation experiments on four representative samples (Sample 00942, 02994, 03813, 04834) by adding Gaussian noise with increasing standard deviation ( $\sigma \in [0, 0.2]$ ).

As visualized in Fig. 9 (and the raw data in Fig. 8), traditional metrics fall into the “Noise Trap”. The curves for AG, SF, and SD (represented by blue, yellow, and purple dashed lines) exhibit a strictly monotonic upward trend across all samples. The EN curve (green dashed line) shows a rapid logarithmic increase. As mentioned in Section III, AG, SF, SD are linearly related with noise. AG and SF are almost equivalent. And, AG score scales proportionally with  $\sqrt{\pi}\sigma$ . SD, however, is a purely linear relationship. So two lines of AG and SF almost coincide and higher than SD.

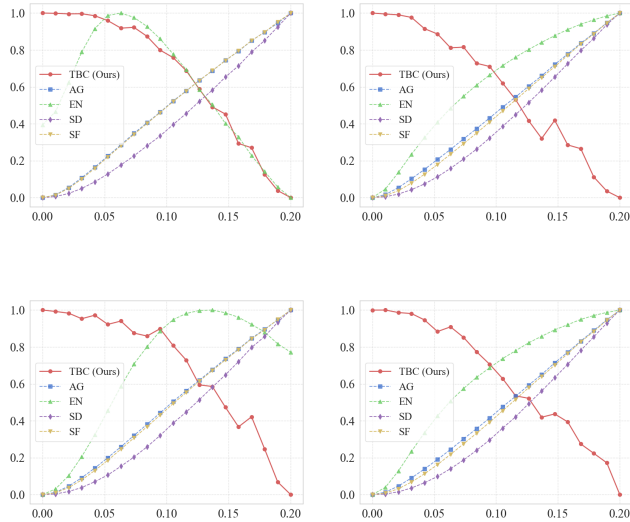


Fig. 8. Single-run noise degradation response curves for four diverse samples. Traditional metrics (AG, EN, SD, SF) monotonically increase, indicating a failure to penalize noise. The TBC curve shows an overall downward trend but exhibits localized fluctuations due to the stochastic nature of noise within small local target regions.

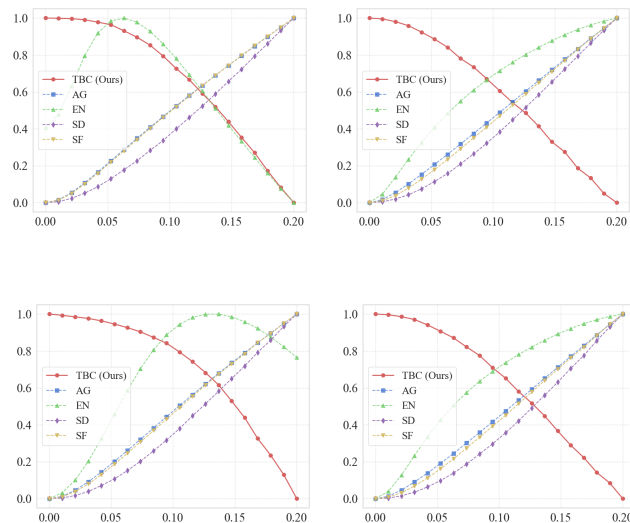


Fig. 9. Monte Carlo averaged noise degradation curves ( $N=50$ ). By averaging out aleatory uncertainty, the underlying statistical trends are revealed. TBC demonstrates a smooth, monotonic decline, confirming its robustness, whereas traditional metrics consistently fall into the “Noise Trap”.

In sharp contrast, the proposed TBC metric (red solid line) demonstrates a consistent monotonic decline across all samples. As noise levels rise, the local background intensity ( $u_{bg}$ ) increases while the target saliency becomes corrupted, leading to a natural penalty in the TBC score. This trend aligns perfectly with human visual perception, confirming TBC’s ability to distinguish signal from noise.

It is worth noting the difference between the single-run results (Fig. 8) and the Monte Carlo averaged results (Fig. 9).

In single-run experiments (Fig. 8), the TBC curves exhibit localized stochastic oscillations (jaggedness), particularly at high noise levels. This phenomenon is not an instability but reflects the local nature of the TBC metric. In the previous paper, it was assumed that the noise follows a normal distribution. So, global metrics average statistics over millions of pixels. According to the law of large numbers, the likelihood of errors becomes very small. But TBC calculates contrast based on small target neighborhoods (often  $\leq 100$  pixels). Consequently, it is highly sensitive to the random polarity of noise.

To mitigate this aleatory uncertainty and reveal the underlying statistical trend, this paper use Monte Carlo mean with 50 repetitions. As shown in Fig. 9, the averaged curves become smooth and strictly monotonic. This proves that while TBC is sensitive to local pixel variations, its statistical expectation is robust and theoretically sound.

Another phenomenon worth noting is that, a counter-intuitive “inverted-U” trend is observed in the EN curve (green line in Fig. 9). Initially, the metric score rises as expected, but it begins to decline after a certain noise threshold. This phenomenon is caused by the Pixel Saturation Effect subject to the limited dynamic range  $[0, 255]$ . As noise intensity escalates, a significant portion of pixel values exceed the physical bounds. The mandatory clipping operation forces these outliers to accumulate at the boundaries (0 and 255), transforming the pixel probability distribution from a spread-out Gaussian-like form to a polarized bimodal distribution. Mathematically, this boundary accumulation reduces the statistical uncertainty of the histogram, paradoxically lowering the entropy score. This non-monotonicity is a critical flaw. It implies that EN suffers from ambiguity, as a single score could correspond to either a moderately detailed image or a heavily saturated noisy image, rendering it unreliable for optimization.

2) *Sensitivity analysis:* The proposed TBC metric relies on a hyperparameter  $k$  (set to 98% by default) to determine the infrared saliency threshold. To investigate the robustness of this choice, this paper analyze the metric’s response across a wide range of percentiles  $k \in [85\%, 99.5\%]$ .

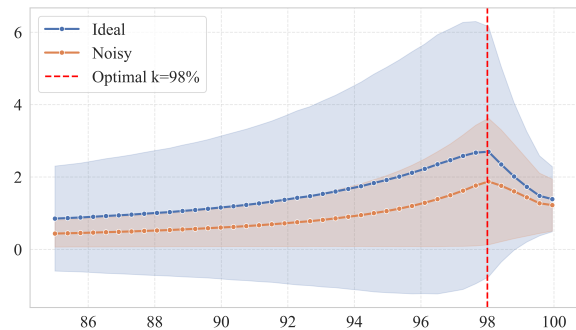


Fig. 10. Threshold sensitivity analysis of the TBC metric. The curves illustrate the TBC scores across varying percentile thresholds for ‘Ideal’ and ‘Noisy’ cases. The distinct inverted-U shape confirms the existence of an optimal operating point. The performance peaks at  $k \approx 98\%$ . Lower thresholds ( $k \leq 95\%$ ) dilute contrast with background noise, while higher thresholds ( $k > 99\%$ ) cause score collapse due to target loss.

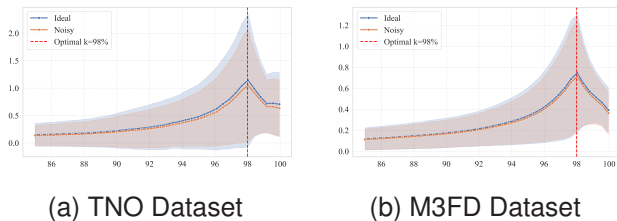


Fig. 11. Cross-dataset parameter sensitivity analysis. Despite differences in sensor resolution and scene content, the TBC scores on both (a) TNO and (b) M3FD datasets exhibit a consistent inverted-U trend, peaking at  $k \approx 98\%$ . This confirms that the proposed threshold is a prior parameter reflecting thermal saliency.

As illustrated in Fig. 10, we plotted the TBC scores for both the ‘Ideal’ and ‘Noisy’ synthetic cases. This curve exhibits a distinct inverted U-shaped distribution.

In the range of  $k \in [85\%, 95\%]$ , the scores rise gradually as the threshold effectively filters out low-intensity background clutter. In the range of  $k \in [95\%, 99\%]$ , the metric reaches a performance plateau, where the TBC scores are maximized. This indicates a “Robust Interval” where the metric effectively captures the target’s core thermal signature while excluding noise. Beyond  $k > 99\%$ , the scores drop sharply. Because the mask becomes too sparse to represent the integrity of the target.

Therefore, while any value within  $[95\%, 99\%]$  yields satisfactory results. But this paper recommend  $k = 98\%$  as the default configuration to as a priori knowledge.

Finally, the DroneVehicle dataset inherently contains targets with a vast dynamic range of thermal intensities. As mentioned above, TBC faithfully records this diversity, resulting in a wide score distribution for clean images.

If the experiment stops here, there will be a suspicion of self-justification. So, this paper extends the sensitivity analysis to two additional benchmark datasets: TNO and M3FD. We apply the same synthetic degradation protocol (Ideal vs. Noisy) across a wide range of thresholds  $k \in [85\%, 100\%]$ .

As visualized in Fig. 11, despite the significant differences in scene content (e.g., soldiers in TNO vs. vehicles in M3FD), the sensitivity curves exhibit a remarkable consistency with the DroneVehicle results. In terms of the results, the conclusions from this additional experiment are consistent with what was described above.

It is noteworthy that the standard deviation (indicated by the shaded region) exhibits a sharp peak coincident with the mean score at  $k = 98\%$ . In particular, in Fig. 11, the blue and red areas almost overlap. TNO and M3FD are classic infrared datasets, and infrared cameras generally have a better signal-to-noise ratio than DroneVehicle. This means that the boundaries between the target and the context are very clear. So, TBC sufficiently sensitive to difference between highly salient targets (e.g., active vehicles) and subtle thermal signatures, thereby maximizing the statistical variance. Therefore, it appears “sharp” rather than “rounded”.

3) *Time complexity*: To validate the real-time capability of TBC for edge-device deployment, this paper benchmarks its execution time against traditional metrics across three

resolutions ( $256^2, 512^2, 1024^2$ ). Similarly, this paper selects the previously mentioned real-world samples and randomly cropped them to the target size for experiments. To eliminate the randomness of experiments, this paper also randomly generates experimental data for comparison.

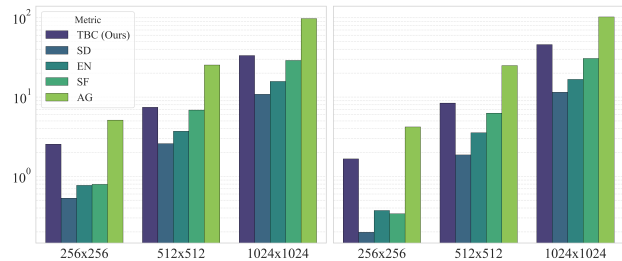


Fig. 12. Dual-validation of computational complexity across different resolutions. The grouped bar charts (log scale) compare the average execution time of TBC against traditional metrics using both (Left) 300 real-world samples and (Right) 100 Monte Carlo simulation runs.

TABLE IV  
DETAILED RUNTIME DATA (UNIT: MS)

Category	Resolution	AG	EN	SD	SF	TBC (Ours)
Real-World	256x256	1.154	0.173	0.094	0.151	0.515
	512x512	8.916	1.333	0.875	2.396	2.100
	1024x1024	<b>70.546</b>	11.962	8.371	21.461	<b>22.670</b>
Monte Carlo	256x256	5.868	0.735	0.585	0.545	2.318
	512x512	26.577	4.244	2.878	7.672	9.536
	1024x1024	<b>100.849</b>	17.043	12.797	30.009	<b>44.554</b>

Fig. 12 corroborates the efficiency of TBC. The trends in the two charts are completely consistent. IV, TBC is faster than AG. In the  $1024^2$  real-world test, TBC requires only 25.73 ms, significantly outperforming AG (78.55 ms). While SD/EN are fast, the previous experiments have shown that they are unusable. Furthermore, 25ms corresponds to 40 FPS, which still meets the real-time requirements. Although SD achieves the lowest latency due to basic matrix operations, it lacks the semantic discriminability required for fusion evaluation.

All in all, TBC performs excellently in low-altitude small target scenarios.

## V. CONCLUSION

In this section, we summarize our work and discuss limitations. Then, we talk about future works.

### A. Conclusion

In this paper, we identify and address a critical evaluation paradox in low-altitude scences — “Noise Trap”. To resolve this, we proposed the Target-Background Contrast (TBC) metric, a physically interpretable standard grounded in Weber’s Law. Unlike traditional metrics, TBC fundamentally shifts the evaluation paradigm from global statistical distribution to local semantic contrast.

The main contributions and findings of this paper are threefold. First, we provide a mathematical proof that gradient-based metrics (e.g., AG, SF) and statistics-based metrics

(e.g., EN, SD) are positively correlated with noise intensity. This proof reveals that the failure of these metrics is not an accidental anomaly but a systematic defect inherent in their mathematical definitions. Second, We conduct extensive synthetic degradation tests and large-scale statistical analysis. TBC demonstrate superior robustness. Third, we provide prior parameter settings suggestions and conduct time complexity experiments. TBC is excellent in computational efficiency, confirming its suitability for real-time deployment on resource-constrained UAV edge devices.

### B. limitations

TBC is not without limitations. The calculation of TBC relies on the semantic prior provided by the infrared sensor. Consequently, in extreme scenarios where the infrared thermal signature is negligible or the sensor is compromised, the generation of the target mask may degrade, potentially affecting the accuracy of the contrast calculation. Additionally, our sensitivity analysis indicates that the threshold parameter  $k = 98\%$  represents an optimal trade-off point. While the metric remains robust within the range of  $[95\%, 99\%]$ , significant deviations from this may lead to either background noise leakage or the loss of target integrity.

### C. Future Work

Building on the research findings of the TBC metric, future work will focus on the following three directions:

- 1) Currently, TBC serves only as a post-processing evaluation metric. We will explore differentiable computation to embed it directly into the loss function of deep learning networks, guiding end-to-end “saliency enhancement” training.
- 2) We will further investigate the quantitative relationship between TBC scores and the performance of target detectors such as YOLO and Faster R-CNN. We aim to explore whether TBC can aid unsupervised fusion networks in improving machine perception accuracy without manual annotation.
- 3) Although this paper focuses on low-altitude reconnaissance, the design philosophy of TBC is equally applicable to fields like medical image fusion and underwater image enhancement. We will verify the universality of TBC in these “small target + strong noise” scenarios.

In conclusion, TBC is not only a more accurate metric but also provides a new optimization direction for solving image fusion challenges in low-altitude environments.

## REFERENCES

- [1] Y. Li, F. Wei, Y. Zhang, W. Chen, and J. Ma, “Hs2p: Hierarchical spectral and structure-preserving fusion network for multimodal remote sensing image cloud and shadow removal,” *Information Fusion*, vol. 94, pp. 215–228, 2023. [Online]. Available: <https://www.sciencedirect.com/science/article/pii/S1566253523000453>
- [2] X. Zhang, “Deep learning-based multi-focus image fusion: A survey and a comparative study,” *IEEE Transactions on Pattern Analysis and Machine Intelligence*, vol. 44, no. 9, pp. 4819–4838, 2022.
- [3] H. Sun, Q. Liu, J. Wang, J. Ren, Y. Wu, H. Zhao, and H. Li, “Fusion of infrared and visible images for remote detection of low-altitude slow-speed small targets,” *IEEE Journal of Selected Topics in Applied Earth Observations and Remote Sensing*, vol. 14, pp. 2971–2983, 2021.
- [4] H. Fang, M. Xia, G. Zhou, Y. Chang, and L. Yan, “Infrared small uav target detection based on residual image prediction via global and local dilated residual networks,” *IEEE Geoscience and Remote Sensing Letters*, vol. 19, pp. 1–5, 2022.
- [5] Y. Li, J. Luo, Y. Zhang, Y. Tan, J.-G. Yu, and S. Bai, “Learning to holistically detect bridges from large-size vhr remote sensing imagery,” *IEEE Transactions on Pattern Analysis and Machine Intelligence*, vol. 46, no. 12, pp. 11 507–11 523, 2024.
- [6] Q. Wang, X. Wang, Q. He, J. Huang, H. Huang, P. Wang, T. Yu, and M. Zhang, “3d tensor-based point cloud and image fusion for robust detection and measurement of rail surface defects,” *Automation in Construction*, vol. 161, p. 105342, 2024. [Online]. Available: <https://www.sciencedirect.com/science/article/pii/S0926580524000785>
- [7] J. Long, Z. Fang, and L. Wang, “Sk-mmfmnet: A multi-dimensional fusion network of remote sensing images and eeg signals for multi-scale marine target recognition,” *Information Fusion*, vol. 108, p. 102402, 2024. [Online]. Available: <https://www.sciencedirect.com/science/article/pii/S1566253524001805>
- [8] X. Zhang, P. Ye, H. Leung, K. Gong, and G. Xiao, “Object fusion tracking based on visible and infrared images: A comprehensive review,” *Information Fusion*, vol. 63, pp. 166–187, 2020. [Online]. Available: <https://www.sciencedirect.com/science/article/pii/S1566253520302657>
- [9] M. Feng and J. Su, “Sparse mixed attention aggregation network for multimodal images fusion tracking,” *Engineering Applications of Artificial Intelligence*, vol. 127, p. 107273, 2024. [Online]. Available: <https://www.sciencedirect.com/science/article/pii/S0952197623014574>
- [10] H. Pan, Z. Jing, H. Leung, and M. Li, “Hyperspectral image fusion and multitemporal image fusion by joint sparsity,” *IEEE Transactions on Geoscience and Remote Sensing*, vol. 59, no. 9, pp. 7887–7900, 2021.
- [11] Z. Zhang, Y. Gao, M. Xiong, X. Luo, and X.-J. Wu, “A joint convolution auto-encoder network for infrared and visible image fusion,” *Multimedia Tools and Applications*, vol. 82, no. 19, pp. 29 017–29 035, Aug. 2023. [Online]. Available: <https://doi.org/10.1007/s11042-023-14758-7>
- [12] X. Luo, J. Wang, Z. Zhang, and X. jun Wu, “A full-scale hierarchical encoder-decoder network with cascading edge-prior for infrared and visible image fusion,” *Pattern Recognition*, vol. 148, p. 110192, 2024. [Online]. Available: <https://www.sciencedirect.com/science/article/pii/S0031320323008890>
- [13] J. Liu, R. Lin, G. Wu, R. Liu, Z. Luo, and X. Fan, “CoCoNet: Coupled Contrastive Learning Network with Multi-level Feature Ensemble for Multi-modality Image Fusion,” *International Journal of Computer Vision*, vol. 132, no. 5, pp. 1748–1775, May 2024. [Online]. Available: <https://doi.org/10.1007/s11263-023-01952-1>
- [14] J. Ma, W. Yu, P. Liang, C. Li, and J. Jiang, “FusionGAN: A generative adversarial network for infrared and visible image fusion,” *Information Fusion*, vol. 48, pp. 11–26, Aug. 2019. [Online]. Available: <https://linkinghub.elsevier.com/retrieve/pii/S1566253518301143>
- [15] H. Li and X.-J. Wu, “CrossFuse: A novel cross attention mechanism based infrared and visible image fusion approach,” *Information Fusion*, vol. 103, p. 102147, Mar. 2024. [Online]. Available: <https://linkinghub.elsevier.com/retrieve/pii/S1566253523004633>
- [16] Z. Wang, Y. Chen, W. Shao, H. Li, and L. Zhang, “Swinfuse: A residual swin transformer fusion network for infrared and visible images,” 2022. [Online]. Available: <https://arxiv.org/abs/2204.11436>
- [17] J. He, X. Luo, Z. Zhang, and X. jun Wu, “Memoryfusion: A novel architecture for infrared and visible image fusion based on memory unit,” *Pattern Recognition*, vol. 170, p. 112004, 2026. [Online]. Available: <https://www.sciencedirect.com/science/article/pii/S0031320325006648>
- [18] Z. Huang, C. Lin, B. Xu, M. Xia, Q. Li, Y. Li, and N. Sang, “T2ea: Target-aware taylor expansion approximation network for infrared and visible image fusion,” *IEEE Transactions on Circuits and Systems for Video Technology*, vol. 35, no. 5, pp. 4831–4845, 2025.
- [19] Z. Wang, Z. Zhang, W. Qi, F. Yang, and J. Xu, “Freggan: Infrared and visible image fusion via unified frequency adversarial learning,” *IEEE Transactions on Circuits and Systems for Video Technology*, vol. 35, no. 1, pp. 728–740, 2025.
- [20] Y. Cao, M. Liu, S. Liu, X. Wang, L. Lei, and W. Zuo, “Physics-guided iso-dependent sensor noise modeling for extreme low-light photography,” in *2023 IEEE/CVF Conference on Computer Vision and Pattern Recognition (CVPR)*, 2023, pp. 5744–5753.
- [21] J. Liu, X. Fan, Z. Huang, G. Wu, R. Liu, W. Zhong, and Z. Luo, “Target-aware dual adversarial learning and a multi-scenario multi-modality benchmark to fuse infrared and visible for object detection,” in *2022 IEEE/CVF Conference on Computer Vision and Pattern Recognition (CVPR)*, 2022, pp. 5792–5801.
- [22] L. Tang, J. Yuan, and J. Ma, “Image fusion in the loop of high-level vision tasks: A semantic-aware real-time infrared and visible image

- fusion network,” *Information Fusion*, vol. 82, pp. 28–42, 2022. [Online]. Available: <https://www.sciencedirect.com/science/article/pii/S1566253521002542>
- [23] L. Tang, Y. Deng, Y. Ma, J. Huang, and J. Ma, “Superfusion: A versatile image registration and fusion network with semantic awareness,” *IEEE/CAA Journal of Automatica Sinica*, vol. 9, no. 12, pp. 2121–2137, 2022.
- [24] H. Fang, M. Xia, G. Zhou, Y. Chang, and L. Yan, “Infrared small uav target detection based on residual image prediction via global and local dilated residual networks,” *IEEE Geoscience and Remote Sensing Letters*, vol. 19, pp. 1–5, 2022.
- [25] Y. Sun, B. Cao, P. Zhu, and Q. Hu, “Drone-based rgb-infrared cross-modality vehicle detection via uncertainty-aware learning,” *IEEE Transactions on Circuits and Systems for Video Technology*, pp. 1–1, 2022.
- [26] H. Li, B. Manjunath, and S. Mitra, “Multi-sensor image fusion using the wavelet transform,” in *Proceedings of 1st International Conference on Image Processing*, vol. 1, 1994, pp. 51–55 vol.1.
- [27] P. J. Burt and E. H. Adelson, “A multiresolution spline with application to image mosaics,” *ACM Transactions on Graphics (TOG)*, vol. 2, pp. 217 – 236, 1983. [Online]. Available: <https://api.semanticscholar.org/CorpusID:316610>
- [28] H. Li and X.-J. Wu, “Densefuse: A fusion approach to infrared and visible images,” *IEEE Transactions on Image Processing*, vol. 28, no. 5, pp. 2614–2623, 2019.
- [29] X. Xie, Y. Cui, T. Tan, X. Zheng, and Z. Yu, “Fusionmamba: Dynamic feature enhancement for multimodal image fusion with mamba,” 2025. [Online]. Available: <https://arxiv.org/abs/2404.09498>
- [30] T. Linfeng, Z. Hao, X. Han, M. Jiayi, and Electronic Information School, Wuhan University, Wuhan 430072, China, “Deep learning-based image fusion: a survey,” *Journal of Image and Graphics*, vol. 28, no. 1, pp. 3–36, 2023. [Online]. Available: <http://www.cjig.cn/zh/article/doi/10.11834/jig.220422/>
- [31] J. W. Roberts, J. A. van Aardt, and F. B. Ahmed, “Assessment of image fusion procedures using entropy, image quality, and multispectral classification,” *Journal of Applied Remote Sensing*, vol. 2, no. 1, p. 023522, 2008. [Online]. Available: <https://doi.org/10.1117/1.2945910>
- [32] C. E. Shannon, “A mathematical theory of communication,” *The Bell System Technical Journal*, vol. 27, no. 3, pp. 379–423, 1948.
- [33] A. Eskicioglu and P. Fisher, “Image quality measures and their performance,” *IEEE Transactions on Communications*, vol. 43, no. 12, pp. 2959–2965, 1995.
- [34] G. Cui, H. Feng, Z. Xu, Q. Li, and Y. Chen, “Detail preserved fusion of visible and infrared images using regional saliency extraction and multi-scale image decomposition,” *Optics Communications*, vol. 341, pp. 199–209, 2015. [Online]. Available: <https://www.sciencedirect.com/science/article/pii/S0030401814011833>
- [35] Y. Han, Y. Cai, Y. Cao, and X. Xu, “A new image fusion performance metric based on visual information fidelity,” *Information Fusion*, vol. 14, no. 2, pp. 127–135, 2013. [Online]. Available: <https://www.sciencedirect.com/science/article/pii/S156625351100056X>
- [36] B. Wang, W. Li, W. Yang, and Q. Liao, “Illumination normalization based on weber’s law with application to face recognition,” *IEEE Signal Processing Letters*, vol. 18, no. 8, pp. 462–465, 2011.
- [37] J. Chen, S. Shan, C. He, G. Zhao, M. Pietikäinen, X. Chen, and W. Gao, “Wld: A robust local image descriptor,” *IEEE Transactions on Pattern Analysis and Machine Intelligence*, vol. 32, no. 9, pp. 1705–1720, 2010.
- [38] Z. Hou and W.-Y. Yau, “Relative gradients for image lighting correction,” in *2010 IEEE International Conference on Acoustics, Speech and Signal Processing*, 2010, pp. 1374–1377.
- [39] G. Zhu, S. Zhang, X. Chen, and C. Wang, “Efficient illumination insensitive object tracking by normalized gradient matching,” *IEEE Signal Processing Letters*, vol. 14, no. 12, pp. 944–947, 2007.
- [40] O. Dabeer and S. Chaudhuri, “Analysis of an adaptive sampler based on weber’s law,” *IEEE Transactions on Signal Processing*, vol. 59, no. 4, pp. 1868–1878, 2011.